A Spherical Active Coded Aperture for 4π Gamma-ray Imaging

Daniel Hellfeld, Paul Barton, Donald Gunter, Lucian Mihailescu, and Kai Vetter

***Abstract*—Gamma-ray imaging facilitates the efficient detection, characterization, and localization of compact radioactive sources in cluttered environments. Fieldable detector systems employing active planar coded apertures have demonstrated broad energy sensitivity via both coded aperture and Compton imaging modalities. However, planar configurations suffer from a limited field-of-view, especially in the coded aperture mode. To improve upon this limitation, we introduce a novel design by rearranging the detectors into an active coded spherical configuration, resulting in a 4π isotropic field-of-view for both coded aperture and Compton imaging. This work focuses on the low-energy coded aperture modality and the optimization techniques used to determine the optimal number and configuration of 1 cm^3 CdZnTe coplanar grid detectors on a 14 cm diameter sphere with 192 available detector locations.**

***Index Terms*—Active coded aperture, gamma-ray imaging, spherical coded aperture, 4π image reconstruction.**

I. Introduction

In addition to the ability to detect and identify radioactive material with gamma-ray detectors, the ability to image radiation distributions in space provides important information that can be utilized in various applications. In the energy regime of tens of keV to a few hundred keV, coded aperture imaging, originally developed by [1], [2], [3], has been widely used in areas such as X-ray and gamma-ray astronomy, medical imaging, and nuclear security. The technique maintains the high angular resolution of a pinhole imager while increasing the image signal-to-noise-ratio (SNR) [4]. Typical systems employ a passive mask (i.e. opaque and transparent non-detector elements) in front of a position sensitive detector. The use of active masks (i.e. masks comprised of detector elements) has been investigated to increase detection efficiency, reduce weight, and enable Compton imaging of higher energy gamma-rays (hundreds of keV to a few MeV) [5], [6]. Recent work has demonstrated real-time 3D imaging with a hand-held, free-moving, dual-mode (coded aperture and Compton imaging) system using room temperature operated CdZnTe (CZT) detectors [7]. Contextual sensors and Simultaneous Localization and Mapping (SLAM) algorithms are used to track the system as it moves through an environment. Scene data fusion [8] is used to improve image accuracy and reduce computational time by constraining the radiation distribution to occupied voxels in the 3D scene model.

The planar mask-detector configuration of the dual-mode imaging systems, however, is prone to imaging artifacts and the coded aperture modality suffers from a limited field-of-view. While passive designs have been considered to overcome this limitation, such as multiple masks [9] and radial hole masks [10], [11], we present an active design by rearranging the active planar system into a spherical active coded aperture to enable both coded aperture and Compton imaging in 4π.

This work focuses solely on the low-energy domain where coded aperture imaging is utilized. In Section II, a description of the overall imaging system is given. In Section III we outline the methods used to generate the system response and in Section IV we present the methods used to optimize the number and configuration of detectors on the sphere. Finally, in Section V, the performance of the 4π image reconstruction is shown for a variety of simulated far-field point sources.

II. Detector Design

The Portable Radiation Imaging Spectroscopy and Mapping (PRISM) detector system is being developed at Lawrence Berkeley National Laboratory (LBNL) and consists of 1 cm^3 CZT crystals with coplanar grid (CPG) readouts [12] distributed among 192 positions on the inner surface of a spherical shell (see Fig. 1). The detector centers form a 14 cm diameter sphere. The shell consists of 6 modular faces each with 32 detector slots. The individual detectors are housed in Lexan housings which snap into the modular faces. Each detector is equipped with an individual ASIC [13], [14] which is connected to the electronics via a flexible circuit on the outer surface of the spherical shell.

An advantage of CPG detectors is the ability to determine the interaction location along the anode-cathode axis, or depth-of-interaction (DOI). In this work, we assume a conservative energy-independent depth-resolution of 2.5 mm, effectively segmenting each detector into four independent $1\times1\times0.25$ cm detectors along the anode-cathode axis.

III. System Response

The system response, C_{ij}, is defined as the probability that a photon from a far-field point source at image pixel j is detected in detector i. This matrix, or an estimate of it, is

Manuscript received September 19, 2017. This material is based on work supported in part by the Department of Energy National Nuclear Security Administration through the Nuclear Science and Security Consortium under Award Number DE-NA-0003180 and the Defense Threat Reduction Agency under Contract Number DTRA10027-19346.

D. Hellfeld is with the Nuclear Engineering Department at the University of California, Berkeley, Berkeley, CA 94720 USA (email: dhellfeld@berkeley.edu).

P. Barton, D. Gunter, and L. Mihailescu are with the Applied Nuclear Physics Program at Lawrence Berkeley National Laboratory, Berkeley, CA 94720 USA (emails: pjbarton@lbl.gov, dgunter@alumni.caltech.edu, lmihailescu@lbl.gov).

K. Vetter is with the Nuclear Engineering Department at the University of California, Berkeley and the Applied Nuclear Physics Program at Lawrence Berkeley National Laboratory, Berkeley, CA 94720 USA (email: kvetter@berkeley.edu).

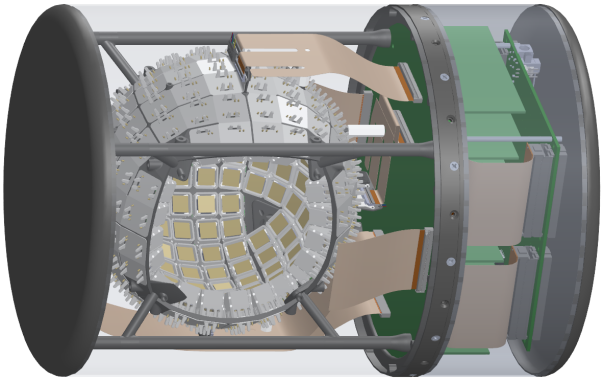

Fig. 1. PRISM prototype design consisting of 6 modular faces each with 32 available detector slots. One face is removed to reveal the gold cathodes on the inner surfaces of the CPG CZT detectors.

crucial to the image reconstruction process. In this work, two approaches were taken to determine the system response.

In the first approach, a Geant4 [15] simulation was developed using a simplified model of the PRISM system (including only the crystals with no dead layer). The far-field image space pixellation was defined on the 2-sphere with the Hierarchical Equal Area isoLatitude Pixelation of a sphere (HEALPix) library [16] with $N_{\text{side}} = 16$ (3072 pixels). When parallelized on 768 CPUs using a high-performance computing cluster (LBNL Lawrencium), the far-field system response of 10^6 system-incident gamma-rays from each of the 3072 source locations can be generated in about 90 seconds.

In the second approach, a graphics-based program was developed using OpenGL to quickly generate the zero-energy (i.e. infinite attenuation and no scattering) system response. OpenGL is widely utilized for fast 2D and 3D graphics rendering using highly-parallelizable GPUs. Given a 3D model (i.e. cubic CZT crystals arranged in a sphere), OpenGL can quickly render an orthographic projection of the geometry (i.e. far-field point source with uniformly spaced parallel rays) including z-buffer occlusion. In our approach, each detector crystal is indexed by a unique 8-bit red color value and DOI is included using a gradient of 8-bit blue values along the anode-cathode axis of each detector. For a given projection (i.e. source location), the red and blue channels in each pixel in the display correspond to a detector index ($1 \rightarrow 192$) and a DOI value ($1 \rightarrow 256$), respectively. The blue values can be binned according to the depth resolution of the detector. Pixels are then histogrammed by color to determine the visible surface area (i.e. effective zero-energy flux) of each detector bin. The system response from all 3072 source locations using a 10^6 pixel display can be generated in under 25 seconds on a single NVIDIA Quadro K1100M graphics card.

The significant decrease in computation time is crucial for the mask optimization (see Section IV) as the 192 available detector locations create an enormous number of possible detector configurations. While a zero-energy system response is unphysical, the results should not differ significantly from those for low-energy photons. At 60 keV, the mean free path in CZT is approximately 0.26 mm (2.6% of the detector thickness) and the ratio of the photoelectric absorption and Compton scattering cross-sections is > 50.

IV. Mask Pattern Optimization

In order to design an optimal mask pattern, a specific metric must first be chosen. There are many important performance characteristics of a 4π imaging system, and the significance of each may vary depending on the application at hand. Therefore, in general, the choice of metric is often unclear.

When designing planar coded apertures, a common metric is the maximization of the SNR of the reconstructed images. The Uniformly Redundant Array (URA) [4] has been shown to optimize this metric [17] while also having constant sidelobes in its periodic autocorrelation function. The URA, however, is only applicable for a limited set of specific aperture sizes and detector geometries. Other mask types also exist, such as the Non-Redundant Array (NRA), Pseudo-Noise Product array (PNP), and Modified Uniformly Redundant Array (MURA) [18], [19]. However, none of these masks have ever been designed for a spherical system. Therefore, an iterative approach similar to [20], [21] based on the heuristic "Great Deluge algorithm" [22] was employed to determine the optimal number and configuration of detectors on the sphere.

To characterize a given mask configuration, we analyzed the ideal imaging performance of far-field point sources at every pixel in the image space. The system response, C_{ij}, was determined using the zero-energy OpenGL approach and images were generated using simple back-projection, $\boldsymbol{C}^T\boldsymbol{C}$, with sensitivity correction. The zero-energy approach was necessary to reduce computational time.

We used 9×10^4 pixels in the OpenGL display, as the addition of more pixels did not significantly change the computed system response ($< 1\%$ fractional change in the L2-norm of the difference). With this many pixels, the system response can be computed in less than 3 seconds.

For this work, we developed a figure-of-merit, Q, designed to maximize sensitivity, enhance localization, and assure uniform performance over 4π. For a given far-field source in pixel j, the sensitivity is defined as the detection probability in any detector, or $S_j = \sum_i C_{ij}$. The localizing performance is described by a signal-to-blur ratio (SBR) of the sensitivity corrected back-projection λ^{BP}, given by

$$\text{SBR}_j = \frac{\lambda_j^{\text{BP}} - \mu(\lambda_{\bar{j}}^{\text{BP}})}{\sigma(\lambda_{\bar{j}}^{\text{BP}})}, \tag{1}$$

where λ_j^{BP} is the image intensity in the true pixel j, and $\mu(\lambda_{\bar{j}}^{\text{BP}})$ and $\sigma(\lambda_{\bar{j}}^{\text{BP}})$ are the mean and standard deviation of the image intensities in all pixels other than j, respectively. The blur in this treatment refers to the systematic geometric blurring inherent in the back-projection. Background noise and counting statistics were not included in the images.

The mean and variance of each metric are then computed over all source locations, j. The figure-of-merit, Q, is defined by averaging the variances and the reciprocal of the means,

$$Q = \frac{\mu(S_j)^{-1} + \sigma^2(S_j) + \mu(\text{SBR}_j)^{-1} + \sigma^2(\text{SBR}_j)}{4}. \tag{2}$$

In every iteration, each term in the numerator of (2) is normalized by its first iteration value. Therefore the initial

value of Q will be equal to 1. The overall minimization of Q will maximize the mean sensitivity and SBR metrics and minimize the variation of the two metrics over 4π.

The optimization begins with a random number of detectors in a random configuration on the sphere. The mask is perturbed by toggling (on/off) a randomly sampled detector location. The figure-of-merit is calculated before and after the perturbation and a Great Deluge acceptance criterion is used. The *water level* (W) was adjusted adaptively at each acceptance according to

$$W_{k+1} = W_k - d(W_k - Q_k)\,, \tag{3}$$

where W_k is the current water level, W_{k+1} is the water level of the next step, Q_k is the current figure-of-merit value, and d is a number between 0 and 1 meant to control the speed of convergence [20]. A value of $d = 0.025$ was used in this work, as smaller values resulted in impractical runtimes.

If all 192 detector slots are toggled without lowering the water level, then two randomly selected detector slots are toggled. If the water level is lowered with the double toggle mode, the procedure reverts back to the single toggle mode. If the water level is not lowered over 1000 iterations, the optimization is stopped.

A. Optimization results

The optimization procedure was performed six times with random initial detector configurations. Due to the large configuration space and our choice of d in (3), we cannot expect the results of the algorithm to be unique. In addition, we do not expect there to be a single mask configuration that significantly outperforms all others. In the several optimizations that were performed, the resulting masks differed slightly in design, however, were similar in both the figure-of-merit and the number of detectors (relative standard deviations of 1.5% and 2.5%, respectively).

Fig. 2 displays the progression of Q as a function of iteration for a single random starting point and Fig. 3 shows the resulting optimized mask. For this particular run, the optimized mask contains 104 total detectors (out of the 192 total available locations). This is slightly larger than a 50% population, determined by [4] to be optimal for the URA. However, because there is a significant amount of open space even in the fully populated geometry due to packing cubes on a sphere and non-zero detector housing thickness, there is no reason to expect that 50% would necessarily be optimal in this case.

Table I shows the individual metrics of Q between the starting and optimized masks. The optimized mask has a higher mean sensitivity (primarily due to the larger number of detectors) and has much more uniform sensitivity over 4π. The optimized mask actually has a slightly lower mean SBR, but the uniformly of the SBR was greatly improved. It is expected that the behavior of these metrics can fluctuate because each were given equal weighting.

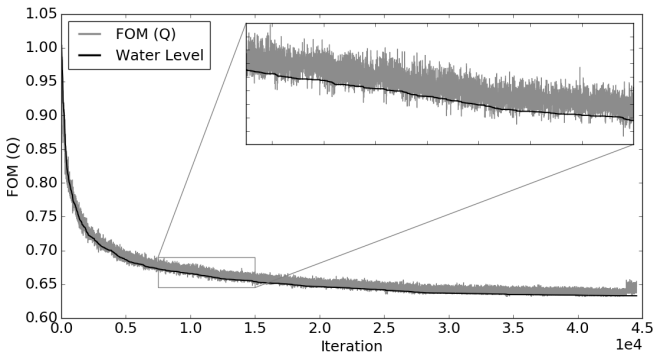

Fig. 2. Minimization of the figure-of-merit Q (defined in Section IV) using the Great Deluge optimization algorithm. At each iteration, the current mask configuration is retained if Q (gray) is below the water level (black).

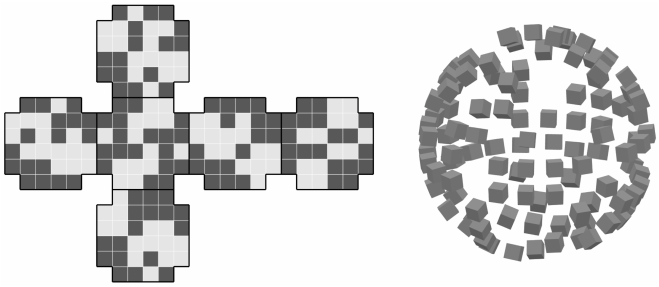

Fig. 3. Optimized mask pattern shown with the six modular faces of the spherical design unfolded into 2D (left) and with the bare crystals in 3D (right). The mask contains 104 detectors out of the 192 available locations.

V. Imaging Performance

The mask configuration was optimized in the previous section using the zero-energy response and ideal counting statistics. In this section, we assess the localization performance of the optimized mask in 4π at multiple energies with limited counting statistics and background noise included.

Geant4 simulations were used to determine the system response of the optimized mask in Fig. 3 to far-field point sources at various energies. The system response was then sampled appropriately to generate data sets with a defined signal to background ratio. Only full-energy absorption events were used to generate the system response and signal data as these are the only events used in the image reconstruction. We assumed a uniformly distributed background in 4π. While unrealistic, this simple background model is sufficient to demonstrate the omnidirectional localization capabilities of the design when random background counts are present.

Images were reconstructed using the Maximum Likelihood Expectation Maximization (MLEM) [23] approach. MLEM is used to improve image quality over simple back-projection, however, due to its iterative nature, comes at the cost of increased computation time. This increase was impractical in optimization procedure (Section IV) but manageable for the small number of reconstructions in the following sections.

TABLE I
Individual sensitivity and SBR metric values in the optimization figure-of-merit, Q.

Mask	Detectors	$\mu(S_j)$	$\sigma^2(S_j)$	$\mu(\text{SBR}_j)$	$\sigma^2(\text{SBR}_j)$
Starting	84	0.366	2.9×10^{-4}	4.883	0.244
Optimized	104	0.431	8.0×10^{-5}	4.562	0.078

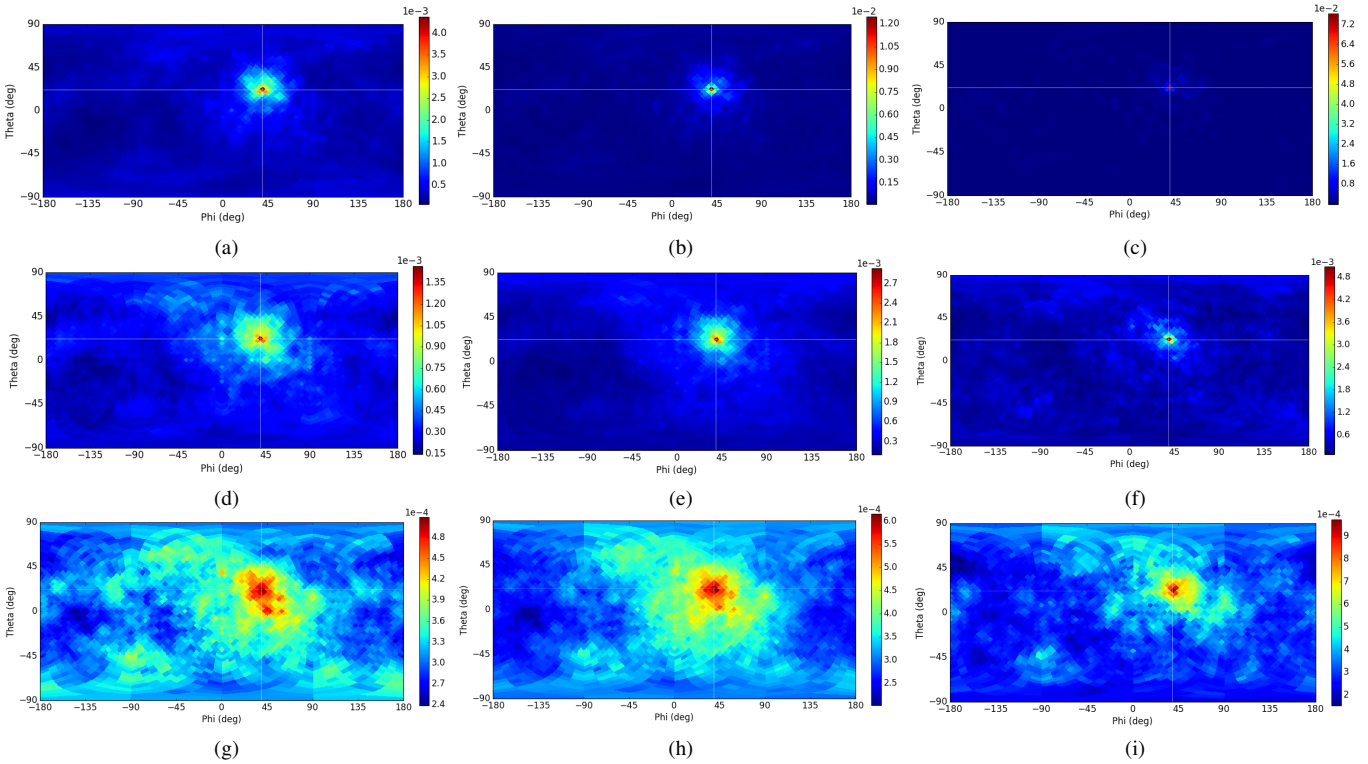

Fig. 4. MLEM image reconstruction (50 iterations) of simulated far-field point sources located at [θ, ϕ] = [22°, 39.5°] in a uniform background. The top, middle and bottom rows correspond to energies of 60, 186, and 356 keV, respectively. The left, middle, and right columns correspond to data without DOI, with all 4 DOI bins, and with only the inner DOI bins, respectively. The images in the left and middle columns used 5000 detected signal counts and 10^4 background counts. Significantly fewer counts were used in the right column images due to the smaller detector volume - (c) 1434 signal and 2892 background, (f) 1179 signal and 2711 background, (i) 1282 signal and 2411 background.

A. *Single far-field point sources of varying energy*

Fig. 4 shows the MLEM image reconstruction of single far-field point sources at energies of 60, 186, and 356 keV. In each case, the true source location is [θ, ϕ] = [22°, 39.5°]. The number of detected signal events in each image is 5000 and the signal to background ratio is 0.5 (10^4 detected background events). The full-energy absorption efficiencies averaged over all 3072 source locations are 54%, 29%, and 8% at 60, 186, and 356 keV, respectively.

The image quality degrades with energy due to the larger mean free path in CZT, reducing the masking effect of the detectors. At 350 keV, the mean free path in CZT becomes larger than the average path length through a cm^3 cube and the photoelectric absorption to Compton scattering ratio is $\sim$0.5. At this energy, the imaging performance should be improved by including or switching entirely to Compton imaging techniques.

The advantage of DOI is shown by comparing the reconstructions with and without DOI. When the detectors are segmented into 4 DOI bins, the amount of information contained in each individual event increases. This results in an improvement of angular resolution and a decrease in noise. The innermost DOI bins will possess more unique coding due to a higher level of occlusion from the outer detectors. Therefore, selecting events only from these bins should facilitate improved image quality. However, because each inner detector bin occupies a much smaller volume, the number of events used in the reconstruction is significantly lower, resulting in some high-frequency noise. Thus this approach may only be practical in high count rate environments. The advantage of DOI tends to decrease as the energy of the gamma-rays increases, again due to the higher level of penetration through the detectors.

B. *Multiple far-field point sources of varying energy*

The angular resolution of the system is expected to be approximately 10°, based on the spherical geometry and detector spacings. Fig. 5 shows the image reconstruction of two equal intensity far-field point sources at energies of 60, 186, and 356 keV separated by an angle of 15°. The total number of detected signal events in each image is 2×10^4 and the signal to background ratio is 1.

We observe similar blurring with increasing energy as in the single source case due to the increased penetration of higher energy gamma-rays. The advantage of DOI is demonstrated here by the ability to resolve the two sources that were otherwise not clearly resolved.

VI. Conclusions

A spherical active coded aperture imaging system is now under development at LBNL in order to resolve the issues of limited field-of-view and imaging artifacts in planar mask-detector systems. A Great Deluge optimization framework has been developed with a fast zero-energy system response

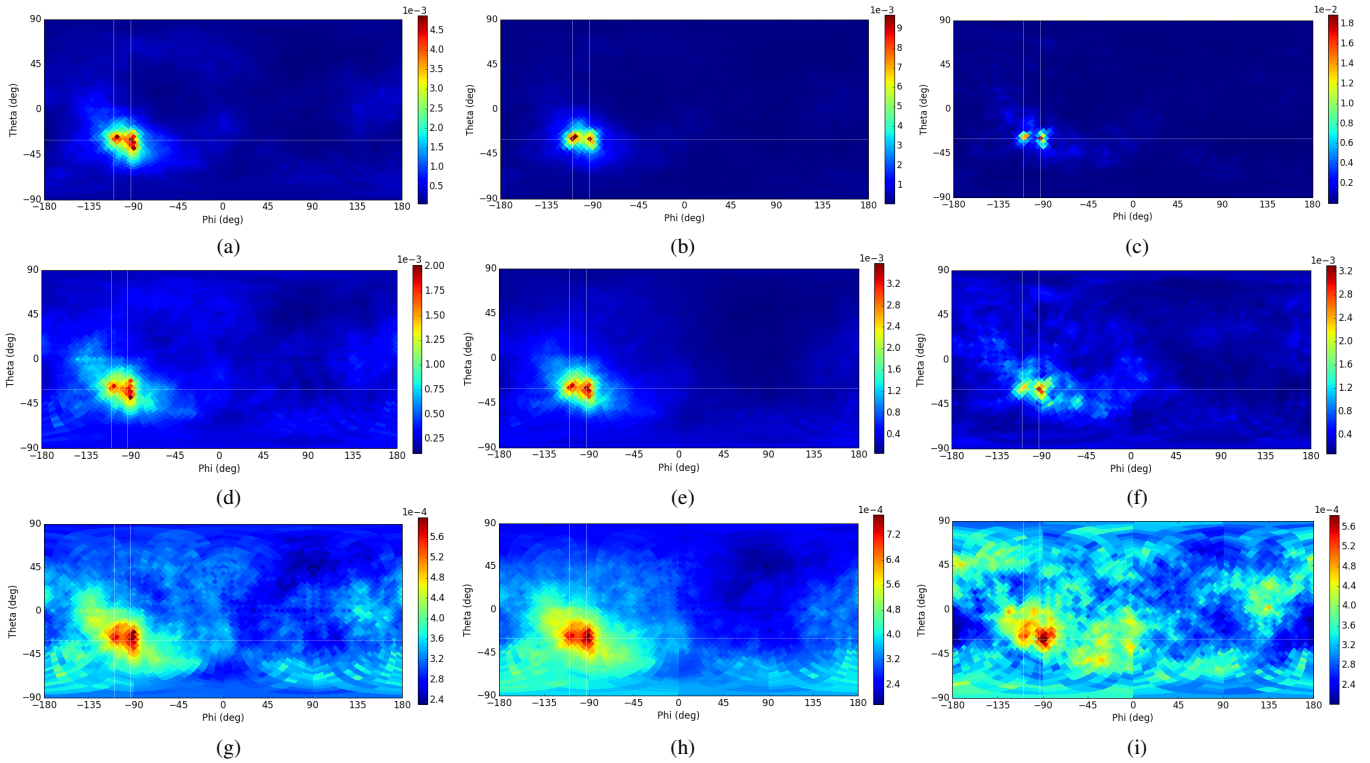

Fig. 5. MLEM image reconstruction (50 iterations) of two simulated equal-intensity far-field point sources separated by 15°. The organization of the images is identical to Fig. 4. The images in the left and middle columns used 2×10^4 detected signal counts and 2×10^4 background counts. Again, significantly fewer counts were used in the right column images due to the smaller detector volume - (c) 5643 signal and 5902 background, (f) 5118 signal and 5184 background, (i) 5070 signal and 5066 background.

generator written in OpenGL. The mask configuration was optimized to maximize sensitivity, localization, and uniformity over 4π. Several optimization were performed with different random starting conditions. The resulting mask were not identical, as expected, but were similar in terms of overall design, imaging performance, and number of detectors.

Equal weightings were given to the three metrics presented here in order to design a balanced system. Further studies could be done to investigate the effects of different weightings, such as in the case where localization may be more important than detection efficiency. Entirely new metrics could also be explored as more specific applications arise.

The 4π imaging performance was shown for simulated far-field point sources at various energies. Depth-of-interaction increased the image quality by improving the angular resolution and reducing the overall noise. The results represent the first successful demonstration of 4π coded aperture image reconstruction using an active spherical array of detectors. When the PRISM system is operational, measurements will be done to validate the simulation results.

Future work will include investigating the capability of 3D imaging when the system is placed in multiple locations as well as continuously moved. Improvements to imaging performance with scene data fusion from contextual sensors such as a visual camera and LiDAR will also be explored.

REFERENCES

[1] L. Mertz and N. O. Young, "Fresnel transformations of images," *Proc. Int. Conf. Optical Instrum. and Techniques*, p. 305, 1961.

[2] R. H. Dicke, "Scatter-hole cameras for X-rays and gamma-rays," *The Astrophysical Journal*, vol. 153, pp. 101–106, 1968.

[3] J. G. Ables, "Fourier transform photography: A new method for X-ray astronomy," *Publications of the Astron. Soc. of Australia*, vol. 1, no. 4, pp. 172–173, 1968.

[4] E. E. Fenimore and T. M. Cannon, "Coded aperture imaging with Uniformly Redundant Arrays," *Applied Optics*, vol. 17, no. 3, pp. 337–347, 1978.

[5] K. P. Ziock, M. Cunningham, and L. Fabris, "Two-sided coded-aperture imaging without a detector plane," *IEEE Nuc. Sci. Symp. Conf. Rec.*, pp. 634–641, 2008.

[6] M. Galloway, A. Zoglauer, M. Amman, S. E. Boggs, and P. N. Luke, "Simulation and detector response for the High Efficiency Multimode Imager," *Nucl. Instrum. Methods A*, vol. 652, pp. 641–645, 2011.

[7] A. Haefner, R. Barnowski, P. N. Luke, M. Amman, and K. Vetter, "Handheld real-time volumetric 3-D gamma-ray imaging," *Nucl. Instrum. Methods A*, vol. 857, pp. 42–49, 2017.

[8] R. Barnowski, A. Haefner, L. Mihailescu, and K. Vetter, "Scene data fusion- real-time standoff volumetric gamma-ray imaging," *Nucl. Instrum. Methods A*, vol. 800, pp. 65–69, 2015.

[9] S. Joshi, "Coded aperture imaging applied to pixelated CdZnTe detectors," Ph.D. dissertation, University of Michigan, 2014.

[10] J. E. Grindlay and J. Hong, "Optimizing wide-field coded aperture imaging: Radial mask holes and scanning," *Proc. SPIE 5168, Optics for EUV X-Ray, and Gamma-Ray Astronomy*, vol. 402, 2004.

[11] J. Hong *et al.*, "Laboratory coded-apeture imaging experiments: Radial hole coded masks and depth-sensitive CZT detectors," *Proc. SPIE 5540, Hard X-Ray and Gamma-Ray Detector Physics VI*, vol. 63, 2004.

[12] P. N. Luke, "Unipolar charge sensing with coplanar electrodes - application to semiconductor detectors," *IEEE Trans. Nucl. Sci.*, vol. 4, p. 207, 1995.

[13] G. D. Geronimo, G. Carini, W. S. Murray, and P. O'Connor, "Front-end ASIC for co-planar grid sensors," *IEEE Trans. Nucl. Sci.*, vol. 52, no. 5, pp. 2003–2008, 2005.

[14] G. D. Geronimo, A. E. Bolotnikov, G. Carini, J. Fried, P. O'Connor, and S. A. Soldner, "Characterization of an ASIC for CPG sensors with grid-only depth of interaction sensing," *IEEE Trans. Nucl. Sci.*, vol. 53, no. 2, pp. 456–461, 2006.

[15] S. Agostinelli *et al.*, "Geant4 - a simulation toolkit," *Nucl. Instrum. Methods A*, vol. 506, pp. 250–303, 2003.
[16] K. M. Górski *et al.*, "HEALPix: A framework for high-resolution discretization and fast analysis of data distributed on the sphere," *The Astrophysical Journal*, vol. 662, no. 2, pp. 759–771, 2005.
[17] E. E. Fenimore, "Coded aperture imaging predicted performance of Uniformly Redundant Arrays," *Applied Optics*, vol. 17, no. 22, pp. 3562–3570, 1978.
[18] E. Caroli, J. B. Stephen, G. D. Cocco, L. Natalucci, and A. Spizzichino, "Coded aperture imaging in X- and gamma-ray astronomy," *Space Science Reviews*, vol. 45, pp. 349–403, 1987.
[19] M. J. Cieslak, K. A. A. Gamage, and R. Glover, "Coded-aperture imaging systems: Past, present and future development - A review," *Radiation Measurements*, vol. 92, pp. 59–71, 2016.
[20] A. Busboom, H. Elders-Boll, and H. D. Schotten, "Combinatorial design of near-optimum masks for coded aperture imaging," *IEEE Int. Conf. Acoust. Speech Signal Process.*, vol. 4, pp. 2817–2820, 1997.
[21] A. Zoglauer, M. Galloway, M. Amman, S. E. Boggs, and P. N. Luke, "HEMI's coded mask: Pattern selection, imaging approaches, and performance," *presented at the IEEE Symposium On Radiation Measurements and Applications (SORMA)*, 2012.
[22] G. Dueck, "New optimization heuristics - the Great Deluge algorithm and the Record-to-Record Travel," *J. of Comp. Phys.*, vol. 104, no. 1, pp. 86–92, 1993.
[23] A. P. Dempster, N. M. Laird, and D. B. Rubin, "Maximum likelihood from incomplete data via the EM algorithm," *J. of the Royal Statistical Society. Series B*, vol. 39, no. 1, pp. 1–38, 1977.